Impact of spatially periodic inhomogeneities on the photon-induced pair creation

M. Jiang ●,[1,2,3] R. Grobe,[4] and Q. Su ●[4]

[1]*School of Science, China University of Mining and Technology, Beijing 100083, China*
[2]*State Key Laboratory for Geomechanics and Deep Underground Engineering,*
China University of Mining and Technology, Beijing 100083, China
[3]*School of Physics, Beijing Institute of Technology, Beijing 100081, China*
[4]*Intense Laser Physics Theory Unit and Department of Physics, Illinois State University, Normal, Illinois 61790-4560, USA*

We study the electron-positron pair-creation process under a combination of a temporally periodic and a spatially periodic field. In the short-time regime where the total yield of created pairs grows linearly, the creation rate due to the temporally oscillating field has been derived analytically. The creation process under a weak spatially periodic field is also found analytically by simplifying the model into sets of four-level systems. We find that the direct energy-conserving transition is negligible; there exist two competing paths that both require symmetric transitions when crossing the energy gap. In the long-time limit, the total creation yield grows in a damped oscillatory fashion and finally relaxes to a specific value as the Rabi oscillations of each four-level system dephase. Compared to the situation with only the temporally periodic field, the spatially inhomogeneous field can increase the production rate due to the opening of new vacuum decay channels.

I. INTRODUCTION

One of the most fascinating aspects of quantum electrodynamics is the prediction that the vacuum can be polarized and generate electron-positron pairs under an extremely strong field [1,2]. In 1951 Schwinger calculated the probability of the vacuum to "break down" under an ultrastrong, static, spatially uniform electric field [3]. The critical value of this process is predicted to be $E_c = 1.32 \times 10^{16}$ V/cm, which requires a laser beam with an intensity of about 10^{29} W/cm^2. Such a tremendously strong intensity is not practical under present experimental conditions. However, due to the continued advancement of the laser technology [4–9], at some point in the future it might be possible that the intensity could reach the critical condition necessary for pair creation.

In the meantime, theoretical studies of the pair-creation process continue. It was pointed out that besides the effect of Schwinger tunneling, which induces pair creation under a steady electric field, an oscillating field can also generate particle pairs due to the multiphoton transitions. The advancement of high-power laser systems has led to numerous theoretical studies investigating the breakdown of the vacuum resulting from the collision of two or more laser beams. Since the groundbreaking multiphoton induced pair-creation experiments at the Stanford Linear Accelerator Center (SLAC) in 1994 [10], laboratories worldwide, including the Extreme-Light Infrastructure [11], the Center for Relativistic Laser Science [12], SLAC [13], the Rutherford Appleton Laboratory [14], and the European X-Ray Free-Electron Laser [15], are actively exploring innovative approaches to probe the quantum vacuum using intense electromagnetic radiation fields. For example, the current energy range of x-ray free-electron lasers (200 eV–11 keV) and the potential upgrade to 25 keV offer exciting prospects for new discoveries.

For a time-dependent and spatially uniform field, the dynamics can be described by a set of two-level systems and the Vlasov equation [16–23]. These can even be solved analytically for some particular fields, because the momentum is strictly conserved. A spatially homogeneous field can be realized at the nodes created by colliding laser pulses [24–27]. However, if an additional spatially inhomogeneous field is considered, these descriptions become invalid, because these inhomogeneities induce additional couplings between states with different momentum and complicate the transition process. For many references on spatial and temporal fields, see the recent reviews [28–32]. To generalize the description of the creation process, the impact of the additional inhomogeneous field needs to be taken into account.

In this paper, to analyze how spatial inhomogeneities affect the pair-creation process, we consider a spatially periodic field in our model, which only allows for transitions with specific momentum differences. The creation process under these combined fields can also be described by the computational quantum field theory, which solves the Dirac equation numerically with full time and space resolution and allows us to compare and accurately gauge the approximations or simplifying assumptions.

This paper is organized as follows. In Sec. II we review the numerical approach to calculate the created electron-positron particle pairs from the solutions of the Dirac equation and present the combination of the external fields discussed in this paper. The short-time behavior of the number of generated pairs is analyzed in Sec. III, along with a strategy of simplifying the system and obtaining the analytical expressions for the total yield and creation rate, with and without the participation of the spatially periodic field. In Sec. IV the long-time behavior of the total yield is discussed, and we present the energy spectrum (Sec. V) as well as the transition

probability due to specific energies (Sec. VI). A conclusion and an outlook are provided in Sec. VII.

II. METHOD AND MODEL

We adopt a one-dimensional model system to describe the pair-creation process by using quantum field theory and solve the Dirac equation numerically [33–36]. The electron-positron field operator can be expanded as $\hat{\Psi}(z,t) = \sum_p \hat{b}_p(t)u_p(z) + \sum_p \hat{d}_p^\dagger(t)v_p(z) = \sum_p \hat{b}_p u_p(z,t) + \sum_p \hat{d}_p^\dagger v_p(z,t)$ through a Bogoliubov transform. Here $\hat{b}_p(t)$, $\hat{d}_p^\dagger(t)$, $\hat{b}_p$, and $\hat{d}_p^\dagger$ denote the time-dependent and -independent annihilation and creation operators for positive or negative states, respectively. The time-dependent operators are linear superpositions of the time-independent operators and can be obtained, e.g., from the corresponding solutions to the Heisenberg operator equations. In our case this formalism is equivalent to transferring the time evolution onto the wave-function states. This (Bogoliubov-transformation-related) formalism was developed first in earlier studies of relativistic heavy-ion collisions, often associated with the work of Greiner's group [37]. The wave functions $u_p(z)$ and $v_p(z)$ are the positive- and negative-energy eigenvectors that can be obtained by solving the force-free Dirac equation in a finite box, while $u_p(z,t)$ and $v_p(z,t)$ are the time-dependent states with positive and negative energies that evolve according to the Hamiltonian of the system. Obviously, in the (computationally impractical) limit of an infinite box, these states can be constructed analytically with a simple z dependence.

The spatial probability density of created pairs is defined as $\rho(z,t) = \langle \text{vac}|[\hat{\Psi}^{(p)}(z,t)]^\dagger \hat{\Psi}^{(p)}(z,t)|\text{vac}\rangle$, where $|\text{vac}\rangle$ denotes the vacuum state, defined by $\hat{d}_p|\text{vac}\rangle = \hat{b}_p|\text{vac}\rangle = 0$. The total number of created electron-positron pairs can be obtained via a space integral of the probability density. Here $\hat{\Psi}^{(p)}$ denotes the positive-energy portion of the field operator. After some derivation, the expression of the total number is obtained as $\int \rho(z,t)dz = \int \sum_p \sum_{p'} |u_p^\dagger(z)v_{p'}(z,t)|^2 dz$, where $v_p(z,t)$ is the time-evolved wave function with $v_p(z,t=0) = v_p(z)$. The two absolute value signs denote the scalar product of the spinor-wave functions. We denote with $N(t)$ the total number of particles per unit length. The time evolution of the function $v_p(z,t)$ follows from the Dirac equation $i\frac{\partial}{\partial t}v_p(z,t) = [c\sigma_1\hat{p}_z - \sigma_1 A(z,t) + \sigma_3 c^2 + V(z,t)]v_p(z,t)$ (in atomic units from now on, where $\hbar = 1$, the mass and electric charge of an electron $m = e = 1$, the fine-structure constant $\alpha = 1/137.036$, and the speed of light $c = 137.036$). In a spatially reduced approach, the role of the usual 4×4 Dirac matrices, often denoted by α_x, α_y, α_z, and β, can be mapped onto the 2×2 Pauli matrices denoted by σ as the spin direction becomes invariant and decoupled. We use the split-operator technique [38–42] and the Fourier transformation to solve it numerically on time and space grids. Our model utilizes periodic boundary conditions and selects reasonable spatial and temporal lengths such that particles that arrive at the boundaries cannot return to the interaction region. The results do not depend on the particular choice of our (purely numerical) parameters such as the spatial grid spacing, the total number of

spatial grid points, or the temporal grid spacings, the extension of the total computational box.

As the decomposition into the electronic and positronic portions of the full field operator is based on the projection onto the force-free states, all time-dependent computed quantities become the true physical observables if the fields were turned off instantly to zero at that particular moment in time. The problem of interpreting particles during the interaction is a very important one and has been discussed already in the literature [43–47].

The external field we study in this paper consists of a combination of two parts, that is, a spatially homogeneous and time-dependent field, which is represented by the vector potential $A(t) = \frac{F_0 c}{\omega}\cos\omega t = A_0\cos\omega t$, and a spatially periodic field introduced by the scalar potential $V(z) = V_0\cos kz$. The spatially homogeneous vector potential can only trigger symmetric transition with identical momentum and opposite energy; the additional spatially inhomogeneous scalar potential breaks the momentum conservation and stimulates asymmetric transitions with different momentum. To simplify the analysis regarding the spatially inhomogeneous field, we chose a periodic scalar potential that only allows transitions with a momentum difference of multiples of k. We investigate the impact of the spatially inhomogeneous field both numerically and derive analytical expressions for the pair-creation rate. While it is more difficult to realize this in terms of any multibeam configuration, it seemed, from a theoretical point of view, more natural for us to be able to consider the space-dependent field as an additional small perturbation first.

III. SHORT-TIME BEHAVIOR OF THE CREATION PROCESS

In this section we discuss the short-time behavior of the pair-creation process under the combined fields, where the total number of created pairs grows linearly over time and therefore can be characterized by a single rate. We will derive analytical expressions for this rate for the larger frequency case, which can be viewed as the complementary expression to the well-known Brezin-Itzykson rate [48] for the low-frequency limit and the zero-frequency limit of Schwinger. We point out, however, that with present laboratory means the high-frequency limit for large intensities is at the moment too demanding to be realized. We also show how these rates are generalized to account for asymmetric momentum transitions induced by spatially inhomogeneous fields.

A. Three rates for the vacuum decay due to a temporally periodic field

We first set $V_0 = 0$ to eliminate the spatially inhomogeneous field and only consider the vector potential $A(t) = A_0\cos\omega t$. In order to compare the numerical results with the rate supported by the analytical formulas of Schwinger [3] and Brezin and Itzykson [48], the total numbers $N(T)$ of created pairs as a function of the frequency ω at a specific time $T = 0.01$ are presented together with the results that are given by the analytical formulas $N(T) = \Gamma T$. For ease of understanding, in Fig. 1 the frequencies are presented in SI units, where α is the fine-structure constant.
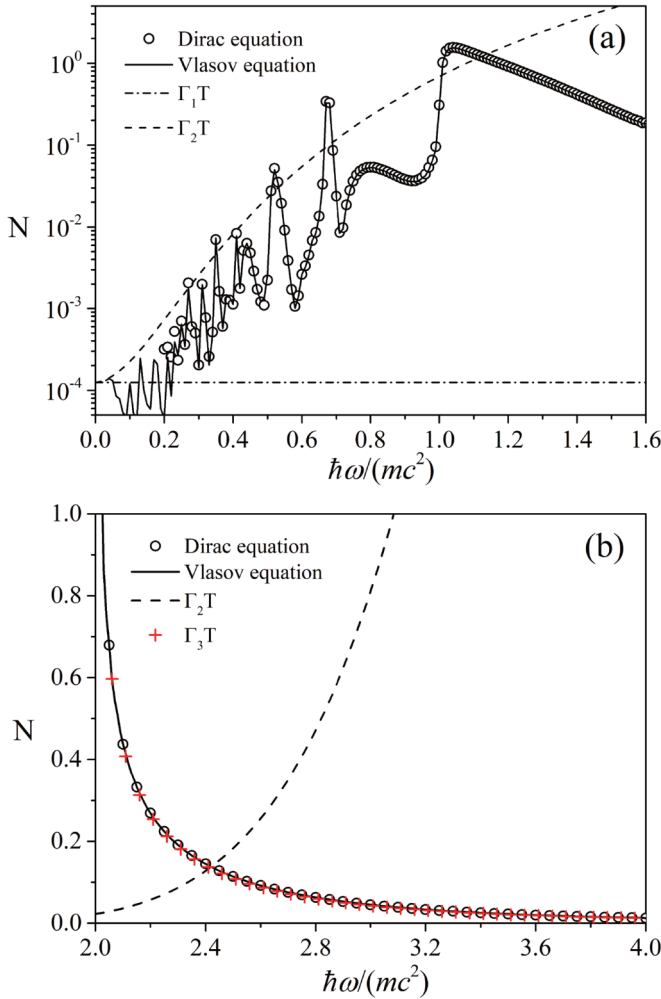
FIG. 1. The total number of created pairs per unit length as a function of the frequency ω at a time $T = 0.01\hbar/(mc^2\alpha^2)$. The amplitude of the electric field of (a) is $F_0 = 0.2c^3m^2/(e\hbar)$ and for (b) is $F_0 = 0.01c^3m^2/(e\hbar)$. The frequency ω is graphed in units of $mc^2/\hbar$. The numerical parameters are box length $L = 12$ a.u., the number of spatial grid points $N_d = 1024$, and the number of time steps $N_t = 12\,000$.

To observe the details of multiphoton transition, a strong intensity of the electric field $F_0 = 0.2c^3$ is used in Fig. 1(a). The simulation results of solving the Dirac equation numerically are presented by the open circles. Multiple peaks found in the figures are attributed to multiphoton transitions with different orders. For example, the rising edge at $\omega = c^2$ corresponds to the threshold of the two-photon transition, and the peak around $\omega = 0.67c^2$ is related to the three-photon transition. Other distinguished peaks for even smaller ω are due to higher orders of photon transitions. As shown in Fig. 1(a), for larger ω, the order of multiphoton transition becomes 1 and the maximum yield increases. For really low frequencies with $\omega < 0.2c^2$, due to the very long optical periods, it is very difficult to calculate the final yield based on finite grid methods. In contrast to fields with larger frequency, this allows us to examine pulses only with a very small number of cycles. For example, with our constant final interaction time of $T = 0.01$ a.u., this would correspond for $\omega = 0.2c^2$ to only

contain three cycles; in that case the impact of the sudden turning on and off of the field becomes very significant. For that reason we start to present the Dirac results (see the open circles) only for frequencies larger than $\omega = 0.2c^2$.

To compare the simulation results with the analytical rates, we first present the yield predicted by Schwinger under a spatially uniform constant field, which should be the limit of $\omega \to 0$ in the figure. Applied to our geometry, the well-known Schwinger rate is given by

$$\Gamma_1 = \frac{F_0}{2\pi}e^{-\frac{\pi c^3}{F_0}}. \tag{1}$$

Therefore the yield is independent of the frequency ω and should be a horizontal line in Fig. 1(a), as shown by the dash-dot line labeled with $\Gamma_1 T$.

The dashed curve with label $\Gamma_2 T$ is provided by the rate of an oscillating uniform field, which increases with ω and approaches $\Gamma_1 T$ when $\omega \to 0$. This rate was derived by Brezin and Itzykson [48] as

$$\Gamma_2 = \frac{F_0}{2\pi}\frac{1}{g(\gamma) + \frac{1}{2}\gamma g'(\gamma)}e^{-\frac{\pi c^3}{F_0}g(\gamma)}, \tag{2}$$

where $\gamma \equiv \omega/F_0$ and the integral is given by

$$g(z) = \frac{4}{\pi}\int_0^1 dy\left(\frac{1-y^2}{1+z^2y^2}\right)^{1/2}. \tag{3}$$

As shown in Fig. 1(a), $\Gamma_2 T$ (the dashed curve) captures the overall growth predicted by the Dirac equation with increasing ω, but it is monotonic and cannot describe the detailed structures of the multiple peaks.

This spatially homogeneous system can also be described exactly by the Vlasov equation [16–23], which can predict the transition between two levels with identical momentum p. The equations are given by

$$\frac{d\rho}{dt} = 2B(t)G(t)$$
$$\frac{dG}{dt} = B(t)[1 - 2\rho(t)] - 2\frac{d\theta}{dt}H(t) \tag{4}$$
$$\frac{dH}{dt} = 2\frac{d\theta}{dt}G(t),$$

with $B(t) = -b_p A(t)$ and $\theta(t) = \int^t d\tau[E_p - a_p A(\tau)]$, here $a_p \equiv cp/E_p = cp/\sqrt{c^4 + c^2p^2}$, $b_p \equiv c^2/E_p$. These equations are solved with the initial condition $\rho(0) = G(0) = H(0) = 0$, where the solution of $\rho(t)$ is the transition probability for each state with momentum p and energy E_p. By summing over p the total yield can be obtained; the result is presented by the solid curve, which matches the predictions of the Dirac equation. This perfect agreement gives credence to the accuracy and reliability of the numerical solution technique of the Dirac equation. We note that the standard Vlasov equation approach can also be expressed in terms of the force-free (nonadiabatic) eigenstates [49,50]. However, for finite pulses they predict the same output after the interaction.

The case $\omega > 2c^2$ for a weak electric field $F_0 = 0.01c^3$ is shown in Fig. 1(b). The open circles and black solid curve represent the result of solving the Dirac and Vlasov equation, respectively, and the black dashed line is $\Gamma_2 T$ according to

Ref. [48]. Obviously, the rate Γ_2 poorly reproduces the simulation results, which means that Γ_2 cannot be applied for large ω. While the low-frequency limits can be approximated by the Schwinger and Brezin-Itzykson rates, an analytical rate for the high-frequency domain has not been discussed in the literature yet. Below we will derive this rate, Γ_3, for frequencies which exceed the energy gap $2c^2$.

In a spatially uniform field $A(t) = A_0 \cos \omega t$, a state with momentum p and negative energy $E_p^- = -E_p$ can only couple to a state with identical momentum p and positive energy $E_p^+ = E_p$. This can be described by the following differential equations for the amplitudes $C_p^+(t)$ and $C_p^-(t)$, assuming $\phi(z,t) = \sum_p C_p^+(t) u_p(z) + \sum_p C_p^-(t) v_p(z)$, where $u_p(z)$ and $v_p(z)$ are the initial positive and negative state with no external field,

$$i\dot{C}_p^+(t) = [E_p^+ - a_p A_0 \cos(\omega t)] C_p^+(t) - b_p A_0 \cos(\omega t) C_p^-(t)$$

$$i\dot{C}_p^-(t) = -b_p A_0 \cos(\omega t) C_p^+(t) + [E_p^- + a_p A_0 \cos(\omega t)] C_p^-(t).$$

$$(5)$$

By applying unitary transformations $C_p^+(t) = e^{-iE_p^+ t} e^{ia_p A_0 \int_0^t \cos(\omega \tau) d\tau} D_p^+(t)$, $C_p^-(t) = e^{-i(E_p^+ - \omega)t} e^{-ia_p A_0 \int_0^t \cos(\omega \tau) d\tau} D_p^-(t)$, the solutions for $C_p^-(0) = 1$ and $C_p^+(0) = 0$ can be written as (see Appendix A for more details)

$$D_p^-(t) = e^{i(E_p^+ - E_p^- - \omega)t/2} \left[\cos\left(\frac{\Omega}{2} t \right) + i(E_p^+ - E_p^- - \omega) \right.$$

$$\left. \times \frac{\sin\left(\frac{\Omega}{2} t \right)}{\Omega} \right]$$

$$D_p^+(t) = \frac{iA_0 b_p}{\Omega} J_0\left(\frac{2a_p A_0}{\omega} \right) e^{i(E_p^+ - E_p^- - \omega)t/2} \sin\left(\frac{\Omega}{2} t \right). \quad (6)$$

Here $\Omega \equiv \sqrt{(E_p^+ - E_p^- - \omega)^2 + A_0^2 b_p^2 J_0^2(\frac{2a_p A_0}{\omega})} = \sqrt{(2E_p - \omega)^2 + A_0^2 b_p^2 J_0^2(\frac{2a_p A_0}{\omega})}$, and J_0 is the zeroth-order Bessel function. Note we have used the identity $e^{i\alpha \sin \omega t} = \sum_{m=-\infty}^{\infty} J_m(\alpha) e^{im\omega t}$ and approximated the summation by the $m = 0$ term. Therefore the total number of created pairs, given by the sum of the transition probabilities over all momenta, can be found as

$$N_3(t) = \sum_{p=-\infty}^{\infty} |D_p^+(t)|^2 = \sum_{p=-\infty}^{+\infty} \frac{A_0^2 b_p^2}{\Omega^2} \sin^2\left(\frac{\Omega}{2} t \right). \quad (7)$$

In the perturbative limit $\frac{2a_p A_0}{\omega} \ll 1$, the term $J_0(\frac{2a_p A_0}{\omega})$ has been replaced by 1 because the Bessel function argument is much smaller than 1. Due to the term $\Omega = \sqrt{(2E_p - \omega)^2 + A_0^2 b_p^2}$, the transition probability is centered at the resonant transition energy $E_p = \omega/2$. Meanwhile, the coefficient b_p changes slowly with p; therefore we replace b_p by a specific value b_{p_0} (p_0 is the momentum for the resonant transition).

To simplify Eq. (7), we replace the summation over the discrete momentum with an integral over Ω by multiplying Eq. (7) with the Jacobian $\mathscr{J} = \frac{\partial n}{\partial p} \frac{\partial p}{\partial E_p} \frac{\partial E_p}{\partial \Omega}$. Here the first factor is $\frac{\partial n}{\partial p} = L/2\pi$ (L is the box length), and $\frac{\partial E_p}{\partial \Omega} = \Omega/(2\sqrt{\Omega^2 - A_0^2 b_p^2})$. For the term $\frac{\partial p}{\partial E_p}$ that is dependent on the energy, E_p can also be substituted by the resonant energy

$\omega/2$, leading to $\frac{\partial p}{\partial E_p} = 1/(c\sqrt{1 - 4c^2/\omega^2})$. As a result, Eq. (7) becomes

$$N_3(t) = \frac{L}{2\pi c \sqrt{1 - 4c^2/\omega^2}} \frac{4F_0^2 c^6}{\omega^4}$$

$$\times \int_{A_0 b_{p_0}}^{\infty} \frac{A_0^2 b_{p_0}^2}{\Omega^2} \sin^2\left(\frac{\Omega}{2} t \right) \frac{\Omega}{\sqrt{\Omega^2 - A_0^2 b_{p_0}^2}} d\Omega. \quad (8)$$

Here we introduced a factor of 2 in Eq. (8) to reflect the fact that the sum over p starts from $-\infty$, while the sum over Ω starts from $A_0 b_{p_0}$. For the limit of $A_0 b_{p_0}$ approaching 0, substituting the formula $\int_0^{\infty} (\sin x/x)^2 dx = \pi/2$, we get a linear time dependence of the total number,

$$N_3(t) \approx \frac{L}{2\sqrt{1 - 4c^4/\omega^2}} \frac{F_0^2 c^5}{\omega^4} t. \quad (9)$$

Therefore the creation rate Γ_3 per unit length for $\omega > 2c^2$ is given by the final expression

$$\Gamma_3 = \frac{1}{2\sqrt{1 - 4c^4/\omega^2}} \frac{F_0^2 c^5}{\omega^4}. \quad (10)$$

In contrast to the monotonically increasing Brezin-Itzykson rate Γ_2, this rate decreases $\sim \omega^{-4}$ with the oscillation frequency ω of the field. Close to the singularity at the threshold, it decreases even more rapidly.

In order to gauge the reliability of the approximations that led to this simple expression, we have compared in Fig. 1(b) the prediction $\Gamma_3 T$ (the red crosses) with the exact data obtained from the simulation based on the Dirac equation. The agreement is superb. In fact, the match is much better than the corresponding one observed for the Brezin-Itzykson rate.

B. Opening of new decay channels due to combined temporal and spatial fields

1. General theory for periodic fields

Due to the presence of an additional spatially inhomogeneous potential, the conservation of momentum is broken, which results in the opening of more vacuum decay channels beyond the ones leading to transition to positive energies centered around $E_p = \omega/2$. In that case, having only two equations, Eq. (5), for each momentum pair becomes insufficient. In fact, for an additional periodic field $V_0 \cos kz$, we need (in principle) an infinite set of coupled equations to describe the dynamics of the state amplitudes (see Appendix B for more details):

$$i\dot{C}_p^+(t) = [E_p - a_p A(t)] C_p^+(t) - b_p A(t) C_p^-(t)$$

$$+ c_{p,p-k} \frac{V_0}{2} C_{p-k}^+(t) + d_{p,p-k} \frac{V_0}{2} C_{p-k}^-(t)$$

$$+ c_{p,p+k} \frac{V_0}{2} C_{p+k}^+(t) + d_{p,p+k} \frac{V_0}{2} C_{p+k}^-(t),$$

$$i\dot{C}_p^-(t) = -b_p A(t) C_p^+(t) - [E_p - a_p A(t)] C_p^-(t)$$

$$- d_{p,p-k} \frac{V_0}{2} C_{p-k}^+(t) + c_{p,p-k} \frac{V_0}{2} C_{p-k}^-(t)$$

$$- d_{p,p+k} \frac{V_0}{2} C_{p+k}^+(t) + c_{p,p+k} \frac{V_0}{2} C_{p+k}^-(t),$$

$$i\dot{C}^+_{p-k}(t) = [E_{p-k} - a_{p-k}A(t)]C^+_{p-k}(t) - b_{p-k}A(t)C^-_{p-k}(t)$$
$$+ c_{p,p-k}\frac{V_0}{2}C^+_p(t) - d_{p,p-k}\frac{V_0}{2}C^-_p(t),$$

$$i\dot{C}^-_{p-k}(t) = -b_{p-k}A(t)C^+_{p-k}(t) - [E_{p-k} - a_{p-k}A(t)]C^-_{p-k}(t)$$
$$+ d_{p,p-k}\frac{V_0}{2}C^+_p(t) + c_{p,p-k}\frac{V_0}{2}C^-_p(t),$$

$$i\dot{C}^+_{p+k}(t) = [E_{p+k} - a_{p+k}A(t)]C^+_{p+k}(t) - b_{p+k}A(t)C^-_{p+k}(t)$$
$$+ c_{p,p+k}\frac{V_0}{2}C^+_p(t) - d_{p,p+k}\frac{V_0}{2}C^-_p(t),$$

$$i\dot{C}^-_{p+k}(t) = -b_{p+k}A(t)C^+_{p+k}(t) - [E_{p+k} - a_{p+k}A(t)]C^-_{p+k}(t)$$
$$+ d_{p,p+k}\frac{V_0}{2}C^+_p(t) + c_{p,p+k}\frac{V_0}{2}C^-_p(t). \tag{11}$$

Here the coupling constants are $c_{p,p\mp k} \equiv [\sqrt{(E_{p\mp k} + c^2)(E_p + c^2)} + \sqrt{(E_{p\mp k} - c^2)(E_p - c^2)}]/(2\sqrt{E_{p\mp k}E_p})$, and $d_{p,p\mp k} \equiv [\sqrt{(E_{p\mp k} + c^2)(E_p - c^2)} - \sqrt{(E_{p\mp k} - c^2)(E_p + c^2)}]/(2\sqrt{E_{p\mp k}E_p})$.

With the spatially periodic field $V(z) = V_0\cos(kz)$ considered, new channels are opened because an initial negative-energy state with momentum p also couples to the negative- and positive-energy states with momentum $p + k$ and $p - k$, which are indicated by the six equations in Eq. (11). It is worth mentioning that if we replace the momentum p in Eq. (11) with $p + k$, then it will couple to states of momentum $p + 2k$ as well, which means states of momentum $p + 2k$ are in principle also coupled to states of momentum p. These couplings can be recognized as higher-order effects of the spatially periodic field and cannot be ignored if the spatially inhomogeneous field is sufficiently strong.

2. Theory for the perturbative limit leading to independent sets of four-level systems

In principle, the equations of Eq. (11) are infinitely coupled for any momentum; however, to analytically solve the process, in the following analysis we choose a relatively weak amplitude V_0 to simplify the transitions to a situation in which only couplings between states with momentum p and $p \pm k$ need to be considered. Energy conservation arguments suggest that any transition energy from a negative-energy state to a positive-energy state should be equal to the energy ω of the photon. In the case of a spatially uniform field that only allows for symmetric transitions, the resonant transition between the states of energy $-E_p$ and E_p, and $E_p - (-E_p) = \omega$ leads to momentum $p_0 = \sqrt{\omega^2/4 - c^4}/c$.

Once a spatially inhomogeneous field breaks the conservation of momentum, arbitrary momentum states p_1 and p_2 of the lower and upper continuum are coupled in an "energy-conserving" fashion, as long as they satisfy $E_{p_2} - (-E_{p_1}) = \omega$. However, for a spatially periodic field, such as $V(z) = V_0\cos kz$, in lowest order of V_0 the initial and final momentum are restricted to $p_2 = p_1 \pm k$.

After considering the extra coupling with states of momentum $p + k$ and $p - k$, the condition of energy conservation is satisfied twice more, with asymmetric transitions from momentum p_- to $p_- + k$, and from p_+ to $p_+ - k$, where p_- and p_+ denote the resonant momenta of the two newly
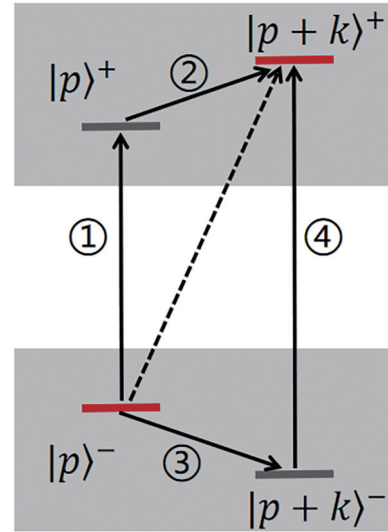

FIG. 2. The transition paths from $|p\rangle^-$ to $|p+k\rangle^+$.

opened channels, respectively. In addition, $p_- + k = p_+$ and $p_+ - k = p_-$. For given k and ω, the two momenta p_- and p_+ can be determined from $E_{p_+} - E_{p_-} = \omega$ and $p_+ - p_- = k$. For the parameters $\omega = 2.5c^2$ and $k = 41.9$, they amount to $p_0 = 102.7$, $p_- = 80.4$, and $p_+ = 122.3$, respectively. Compared with the case of a spatially uniform field, which only has one symmetric resonant transition, the combined field has three resonant transitions, as two more asymmetric channels opened. Note that the symmetric transition involving states with identical momentum is independent of the asymmetric transition involving states with momentum difference of k. Therefore they contribute to the total yield separately.

To discuss the influence of the spatially inhomogeneous field on the creation process, we focus on transitions between states with momentum centered around p_- and p_+, because they account for the vast majority of the total yield in addition to the transitions from p_0 to p_0 for $V_0 = 0$. Due to the discrete grids in the numerical simulation, the momentum cannot be exactly $p_- = 80.4$, so we choose a negative-energy state of momentum $p = 80.1$ near p_- and discuss the coupling to the positive-energy state with momentum $p + k$ around p_+. In that case, the infinitely coupled equations, Eq. (11), are reduced to four equations which represent the couplings of four levels as shown in Fig. 2. The vertical direction reflects the energy E of the state, and the gray shaded areas are the continuous positive and negative states, respectively. To simplify the discussion, we label the negative- and positive-energy states with momentum p as $|p\rangle^-$, $|p\rangle^+$, and momentum $p + k$ as $|p+k\rangle^-$, $|p+k\rangle^+$, respectively.

As the coupling strengths between these four states differ significantly in magnitude, the initial state $|p\rangle^-$ is coupled via two mutually interfering pathways (via transitions ① and ② or via ③ and ④) to the final state $|p+k\rangle^+$. Quite interestingly, according to our results (illustrated in Fig. 3), the direct and fully resonant path (dashed line) between these two states is negligible. Also, the transition ① in Fig. 2 from $|p\rangle^-$ to $|p\rangle^+$ is an off-resonance transition because p differs significantly from the optimal momentum for symmetric resonant transition, which is $p_0 = 102.7$.
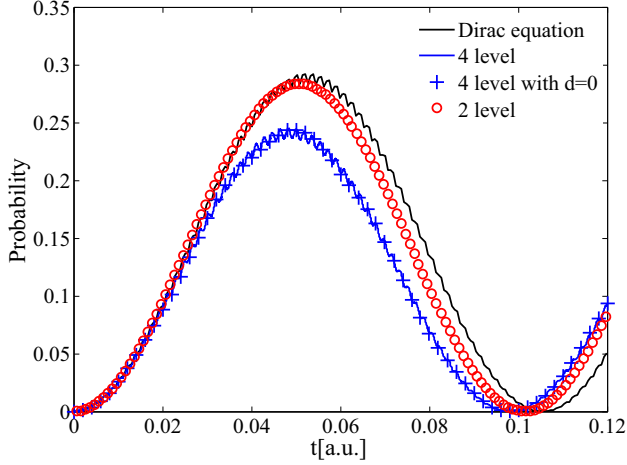
FIG. 3. The time evolution of the transition probability $|C_{p+k}^+(t)|^2$ with specific momentum $p = 80.1$, $k = 41.9$, and $V_0 = 0.01c^2$. Parameters for the oscillating field are $F_0 = 0.1c^3$ and $\omega = 2.5c^2$.

The time evolution of the transition probability under a weak amplitude $V_0 = 0.01c^2$ is shown in Fig. 3. We show the time evolution of $|C_{p+k}^+(t)|^2$ from the numerical calculation of the four differential equations for the states $|p\rangle^-$, $|p\rangle^+$, $|p+k\rangle^-$, and $|p+k\rangle^+$ in Eq. (11) by setting $C_p^-(0) = 1$, $C_p^+(0) = C_{p+k}^-(0) = C_{p+k}^+(0) = 0$. This is illustrated by the blue solid curve in Fig. 3. The black solid curve is the numerical result of solving the Dirac equation. Both the period and the amplitude of the simulated results are fairly well recovered by the solution of the four differential equations. The oscillatory data in Fig. 3 with a maximum value of about 0.3 suggests Rabi oscillations take place between states that are in near resonance with the external field. In Eq. (11) the coefficients in front of the amplitudes indicate the strength of coupling between the corresponding states. For the parameters in Fig. 3, $b_p A_0 = 648.5$, $b_{p+k} A_0 = 561$, $c_p \frac{V_0}{2} = 93.4$ and $d_p \frac{V_0}{2} = 12$. The last term is the transition strength between $|p\rangle^-$ and $|p+k\rangle^+$, and is relatively small compared to other coefficients, suggesting the irrelevance of the direct and fully resonant path. In order to test this, we set $d_p = 0$ and solve the differential equations again; the results remain unchanged, as shown by the blue crosses in Fig. 3. Therefore a transition that starts from $|p\rangle^-$ has only two mutually interfering pathways to the final state $|p+k\rangle^+$. Notice that in both paths there is a symmetric transition with identical momentum: $|p\rangle^-$ to $|p\rangle^+$ ① or $|p+k\rangle^-$ to $|p+k\rangle^+$ ④, which indicates that to cross the energy gap, a symmetric momentum transition is preferred.

The terms $d_{p,p-k} C_{p-k}^+(V_0/2)$ and $d_{p,p+k} C_{p+k}^+(V_0/2)$ contribute in principle to the evolution of dC_p^+/dt in the first equation of Eqs. (11) and can formally couple the (initially populated) lower state with amplitude C_{p+k}^- and momentum $p+k$ into the upper continuum with amplitude C_p^+. However, as the dynamically relevant couplings in the energy-level diagram Fig. 2 indicates, the direct population transfer from this level is dynamically not so important in lowest order. Besides, this term is independent of the electric field associated with the temporal inhomogeneity proportional to A_0, and its exis-

tence stems from the special additive form of the configuration we chose.

3. Decay rate for V_0-induced non-momentum-conserving transitions

In general, a four-level system cannot be solved analytically. However, as $|p\rangle^-$ and $|p+k\rangle^+$ carry most of the population, we adopt an adiabatic approximation of the intermediate states $|p\rangle^+$ and $|p+k\rangle^-$, neglecting the terms involving $d_{p,p-k}$ and $d_{p,p+k}$, thus further simplify the system into a two-level system (see Appendix C for more details):

$$
\begin{aligned}
i\dot{D}_p^-(t) &= Q D_p^-(t) + R D_{p+k}^+(t) \\
i\dot{D}_{p+k}^+(t) &= R D_p^-(t) + S D_{p+k}^+(t),
\end{aligned}
\tag{12}
$$

where the expressions for the new effective coupling constants Q, R, and S are

$$
Q = \frac{b_p^2 A_0^2}{4(\omega - 2E_p)} + \frac{c_{p,p+k}^2 V_0^2}{4(E_p - E_{p+k})}
$$

$$
R = -\frac{c_{p,p+k} V_0}{4} \left(\frac{b_p A_0}{\omega - 2E_p} + \frac{b_{p+k} A_0}{E_{p+k} - E_p} \right)
\tag{13}
$$

$$
S = (E_p + E_{p+k} - \omega) + \frac{b_{p+k}^2 A_0^2}{4(E_{p+k} - E_p)} + \frac{c_{p,p+k}^2 V_0^2}{4(\omega - 2E_p)}.
$$

Note that the effective coupling R between $|p\rangle^-$ and $|p+k\rangle^+$ clearly displays the coexistence of two paths. It is given by the sum of the two terms, which both contain the factor $c_{p,p+k} V_0$ corresponding to the transitions 2 or 3 between $|p\rangle$ and $|p+k\rangle$ as well as the factor $b_p A_0$ and $b_{p+k} A_0$ corresponding to the symmetric momentum transitions 1 or 4, as pointed out in Fig. 2.

The analytical solutions for $D_p^-(0) = 1$ and $D_{p+k}^+(0) = 0$ can be obtained as

$$
D_p^-(t) \simeq e^{-\frac{i}{2}(Q+S)t} \left[\cos(\Omega_s t/2) + \frac{i(Q-S)}{\Omega_s} \sin(\Omega_s t/2) \right]
$$

$$
D_{p+k}^+(t) \simeq -i e^{-\frac{i}{2}(Q+S)t} \frac{2R}{\Omega_s} \sin(\Omega_s t/2).
\tag{14}
$$

Here $\Omega_s = \sqrt{4R^2 + (Q-S)^2}$. This spatially dressed Rabi frequency Ω_s approaches $\Omega_s \to b_p^2 A_0^2 / [4(\omega - 2E_p) + (E_p + E_{p+k} - \omega)]$ in the limit $V_0 \to 0$. We graph the analytical solution Eq. (14) in Fig. 3 as the red open circles, which reproduces the time-dependent behavior of the simulation results very well. We do not have any clear explanation as to why a theory based on more approximations seems to match the data better than one with less approximations.

To discuss the total yield introduced by the spatially inhomogeneous field, we need to sum over all momenta of Eq. (14). The factor of 2 accounts for the additional transition from $|p\rangle^-$ to $|p-k\rangle^+$, which produces an identical yield as the transition from $|p\rangle^-$ to $|p+k\rangle^+$ as discussed above. Then the expression of the total number due to the spatially inhomogeneous field can be obtained,

$$
N_4(t) = 2 \sum_{p=-\infty}^{+\infty} |D_{p+k}^+(t)|^2 = \sum_{p=-\infty}^{+\infty} \frac{8R^2}{\Omega_s^2} \sin^2(\Omega_s t/2).
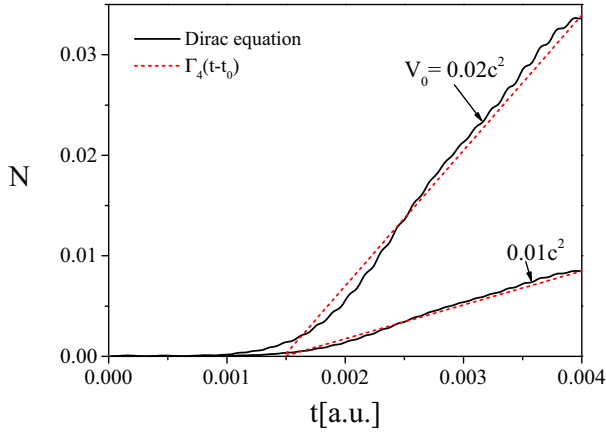\tag{15}
$$

FIG. 4. The time evolution of the yield caused by the spatially periodic field for different strengths of V_0 with $k = 41.9$. Parameters for the temporally oscillating field are $F_0 = 0.1c^3$ and $\omega = 2.5c^2$.

This equation is functionally very similar to Eq. (7). By adopting the same procedure of obtaining the early-time rate as discussed in Sec. III A, the creation rate due to the spatially inhomogeneous field is given by

$$\Gamma_4 = \frac{R_0^2}{c\sqrt{1 - 4c^2/\omega^2}}. \tag{16}$$

Here R_0 denotes the coupling constant R evaluated for resonant momentum $p_- = 80.4$, where the transition probability is maximum. While Γ_4 shares the same threshold singularity as Γ_3, it is proportional to $(A_0 V_0)^2$ and has a nontrivial dependence on the spatial scale k.

To verify the analytical results, we subtract the contributions to the yield associated with the symmetric momentum transitions from the simulation results and compare the time evolution of the yield caused by the spatially periodic field individually with the above analysis in Fig. 4.

The black solid lines are the simulation results; here we present two different amplitudes of the periodic field, $V_0 = 0.01c^2$ and $V_0 = 0.02c^2$. Notice that the yields of the created pairs do not start growing right after the turn-on of the combined field, which indicates that the impact of the spatially inhomogeneous field is delayed. Then the yields grow linearly with time. The straight red dashed lines are predictions according to the analytical rate Γ_4 provided by Eq. (16). A delay time $t_0 = 0.0015$ is chosen manually in order to match the solutions of the Dirac equation, and the red dashed lines both agree well with the simulation results. However, we presently still do not have any explanation for the physical mechanism for the observed delay.

As several prior studies have suggested that the spatial degree of freedom of an external field typically decreases the overall pair-creation efficiency, we have to examine the nature of the predicted increase for our system in more detail. The key question we must address is whether our increase due to the addition of the spatially inhomogeneous field is trivial and can be simply explained in terms of the increase of the resulting total electric field or energy associated with $A(t)$ and $V(z)$. In other words, for a fair comparison we have to relate the pair-creation rate triggered by the dual space-time caused yield triggered by both $A(t)$ and $V(z)$ with an exclusively

temporally induced rate [only due to $A(t)$] under conditions of the same overall intensity or same electric field. As in many dynamical systems driven by time-dependent external forces, the total available energy provided is usually the most relevant quantity. We felt that keeping the intensity constant provides the most natural and fair comparison between the effects of both forces, compared to considering other powers of the force amplitude. To do so we can use the analytical expressions for two rates $\Gamma_3(F_0)$ [Eq. (10)] and $\Gamma_4(F_0, V_0)$ [Eq. (16)] as derived above.

The total electric field associated with both excitation modes, defined as $F(z, t) \equiv -A(t)/c - V'(z)$, amounts to $F(z, t) = F_0 \sin(\omega t) + V_0 k \sin(kz)$. We can define a space-time-averaged intensity as the double integral $I \equiv (ZT)^{-1} \int dz \int dt F^2(z, t)$, where the two scales are given by $Z = 2\pi/k$ and $T = 2\pi/\omega$. We obtain for this intensity $I = (F_0^2 + V_0^2 k^2)/2$, which means that two excitation forces given by the two amplitudes $[F_0, V_0]$ and alternatively by the two amplitudes $[F_{\text{single}} \equiv (F_0^2 + V_0^2 k^2)^{1/2}, V_{\text{single}} = 0]$ have the same effective intensity I.

It turns out that the observed total vacuum decay rate $\Gamma_3(F_0) + \Gamma_4(F_0, V_0)$ exceeds $\Gamma_3(F_{\text{single}})$, and therefore the spatial field enhances the yield. By applying the parameters used in Fig. 4, we can calculate the rate caused solely by $A(t)$ as $\Gamma_3(F_0) = 1098$. When $V_0 = 0.01c^2$, the value of $\Gamma_4(F_0, V_0)$ is 7.4. In this case we can obtain $\Gamma_3(F_{\text{single}}) = 1099$ and the sum of $\Gamma_3(F_0)$ and $\Gamma_4(F_0, V_0)$ is 1105. When $V_0 = 0.02c^2$ is increased to $\Gamma_4(F_0, V_0) = 29.7$, we can observe $\Gamma_3(F_{single}) = 1102$, while the sum of $\Gamma_3(F_0)$ and $\Gamma_4(F_0, V_0)$ becomes 1128. This means that the observed increase of the yield is indeed an enhancement for the fixed intensity case.

We briefly describe the result for another comparison where we kept maximum field strength $F_{\max} = F_0 + V_0 k$ fixed instead of maintaining the space-time integral $I = (F_0^2 + V_0^2 k^2)/2$ constant. In this scenario the parameters used are the same as those in Fig. 4, with $V_0 = 0.01c^2$, resulting in a corresponding maximum electric field strength of $F_{\text{single}} = F_0 + V_0 k (= 0.103058c^3)$. The field associated with the single field denoted as $\Gamma_3(F_{\text{single}})$ is found to be 1166, which is larger than the actual rate 1105. This suggests that in the second scenario, where $F_{\max}$ is kept constant, we do not observe any enhancement. Therefore, if the spatial field can actually enhance the yield or not depends on the details on how this comparison is performed.

IV. LONG-TIME BEHAVIOR

In this section we discuss the long-time behavior of the total yield $N(t)$ for different amplitudes of the spatially periodic field V_0. In Fig. 5 the black solid curves are the simulation results of the Dirac equation. When $V_0 = 0$ and only the spatially uniform field is considered, the total yield first experiences a linear growth at the early stage as we discussed in Sec. III A, and then it oscillates with the Rabi frequencies of the two-level systems. Obviously, the oscillation fades as time evolves and the Rabi oscillation of each transition dephases. In the long-time limit, it saturates and approaches the horizontal black dotted line, which is given by Eq. (7) with the term $\sin^2(\frac{\Omega}{2}t)$ replaced by 0.5. Also, the analytical total yield indicated by Eq. (7) is shown as the
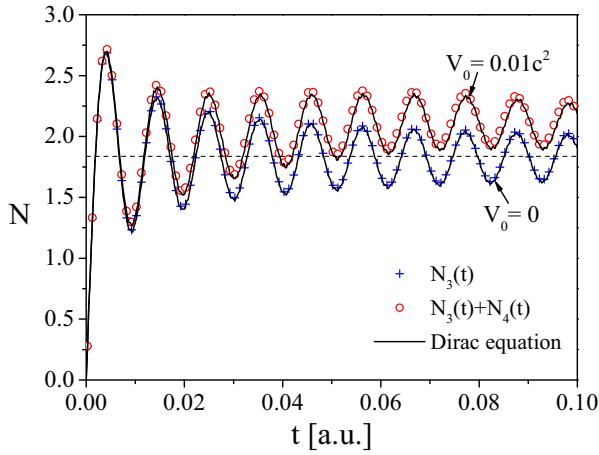
FIG. 5. The time evolution of the total number of pairs per unit length for different strengths of V_0 with $k = 41.9$. Parameters for the temporally oscillating field are $F_0 = 0.1c^3$ and $\omega = 2.5c^2$.

FIG. 6. The final total pair-creation yield $N(T)$ as a function of the frequency ω at a time $T = 0.03$. The amplitude of the field is $F_0 = 0.3c^3$, and $k = 21$.

blue crosses, which are in good agreement with the simulation results.

For a weak field $V_0 = 0.01c^2$, the simulation result $N(t)$ is shown by the black solid curve in Fig. 5, which has the same shape as for $V_0 = 0$ but with some extra pair production. In addition to pairs produced by the spatially uniform field, the newly opened channels due to the spatially periodic field create additional particle pairs and lead to an increase of the total yield. For the contribution to the total yield provided by the dominant symmetric transition, we can adopt the results of Eq. (7) because such a weak field $V_0 = 0.01c^2$ does not affect this transition. For the part provided by the asymmetric transition, the analysis in Sec. III B is applicable, where Eq. (15) is the extra yield caused by the spatially inhomogeneous field.

According to the discussion in Sec. III, the symmetric transition only involves states with identical momentum p and is optimal at $p_0 = \sqrt{\omega^2/4 - c^4}/c$, while the asymmetric transitions are about states of momentum p and $p \pm k$ and are most probable at p_- or p_+. Hence, these two sets of systems do not couple with each other and contribute to the total yield separately. The red open circles in Fig. 5 represent the summation of the analytical results given by Eqs. (7) and (15), which again agrees with the simulation results very well.

The nonoscillatory long-time behavior reflects the fact that each transition has its own Rabi frequency, which then gets out of phase with other transitions and therefore cancels out. As we suggested above, however, in the short-time limit corresponding to finite pulses, the number of particle pairs should still reflect the Rabi oscillations. Especially for early times the small difference between the Rabi frequencies makes these transitions oscillate almost fully in phase.

Even if we were to consider a smoothly-turned-off pulse envelope, the oscillations in the final particle yield as a function of the total pulse duration are still present for short pulses. To test this we have repeated our simulations but replaced the abrupt turn-off with an added $\sin^2$ envelope turn-off of various durations. The chosen turn-off times varied between one and ten optical cycles of the field. As expected, the Rabi oscillations in the final yield as a function of the total pulse duration were still present. While the amplitude was nearly
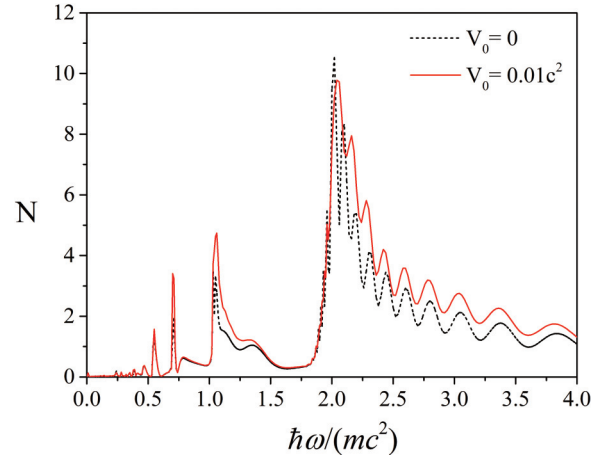
unchanged, the phase (timing of maximal amplitude) was very slightly shifted, reflecting the expected overall longer effective interacting time associated with those cases where the turn-off period was chosen longest. In Fig. 6 we present the final pair-creation yield at time $T = 0.03$ as a function of the frequency ω. The black dashed curve is for $V_0 = 0$, and the red curve is for $V_0 = 0.01c^2$ with $k = 21$. In contrast to Fig. 1(b), where the total yield decreases monotonically, here the total number oscillates. In Fig. 1 the yield grows linearly at early times, while in Fig. 6 for longer time the yield oscillates with a period that depends on the frequency ω. For each frequency the yield oscillates with time as shown in Fig. 5, with a cycle that is related to the frequency. Near the threshold these oscillations become more severe. Therefore, for different frequencies the phases are different at the same observing time of $T = 0.03$, resulting in the physical peaks seen in the graph.

For the red curve for $V_0 = 0.01c^2$ it shows a similar oscillating behavior as the black dashed curve due to the same vector potential. The yield increment is caused by the newly opened channels triggered by the spatially inhomogeneous field. The red curve in Fig. 6 is well described by the analytical theory derived above. The final and unambiguous particle yield pair creation is obtained after the pulse is suddenly switched off at time $t = T$. Therefore it is not a surprise that this graph still reflects the temporal oscillations already displayed in Fig. 5 for $T > 0.03$, except that here they are manifest as oscillations as a function of the laser frequency. Had we chosen a sufficiently longer interaction time, these oscillations in Fig. 6 would have disappeared.

V. ENERGY SPECTRA

In this section we discuss the pair-creation process from the perspective of the energy spectra defined as $\langle vac| b_p^\dagger(t) b_p(t) |vac \rangle$, which is obtained by solving the Dirac equation numerically. In Fig. 7 we present the energy spectra for zero, weak, and large amplitudes of the periodic potential, $V_0 = 0$ for (a), $V_0 = 0.01c^2$ for (b), and $V_0 = 0.05c^2$ for (c). In Fig. 7(a) where the spatially inhomogeneous field is absent, the envelope of the energy spectrum has only one peak centered at energy $E_p = \omega/2 = 1.25c^2$ and $p_0 = 102.7$. It is
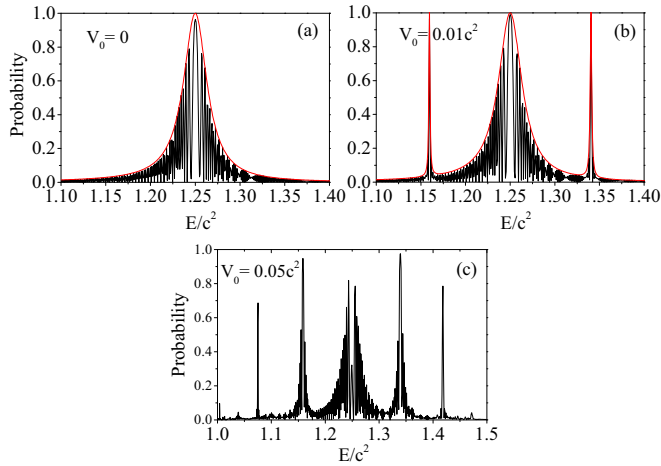
FIG. 7. The energy spectrum of the created positrons at time $T = 0.1$ for $V_0 = 0$ (a), $V_0 = 0.01c^2$ (b), and $V_0 = 0.05c^2$ (c) with $k = 41.9$. Parameters for the temporally oscillating field are $F_0 = 0.1c^3$ and $\omega = 2.5c^2$.

associated with the on-resonant transition and $E_p - (-E_p) = \omega$. We also plot the amplitude of the analytical solution $|D_p^+(t)|^2$ in Eq. (6) as the red curve, which depicts the profile of the peak perfectly. The fine structures inside the peak oscillate with time, which can also be described by Eq. (6).

If we include a weak, spatially periodic field with strength $V_0 = 0.01c^2$ in Fig. 7(b), the structure of the middle peak remains basically unchanged. In addition, there appear two new peaks due to the newly opened decay channels. The asymmetric transitions from $|p\rangle^-$ to $|p \pm k\rangle^+$ are now also allowed. For the parameters $\omega = 2.5c^2$ and $k = 41.9$, the transition should be maximized at $p_- = 80.4$ with $E_{p_-} = 1.16c^2$ and $p_+ = 122.3$ with $E_{p_+} = 1.34c^2$, which is exactly the center of the two new peaks in Fig. 7(b). We also portray the profile of the peaks with the amplitude of the analytical solution in Eq. (14), as shown by the red curve in Fig. 7(b). The analytical solution predicts not only the center but also the widths of the peaks and all the oscillatory details, as presented in Fig. 7(b). Note that the side peaks are relatively narrow and located far from the main peak as we choose a large $k = 41.9$. Therefore, in order to recover the total number of pairs one can simply add up Eqs. (7) and (15) as we did in Sec. IV. However, the side peaks will become closer to the center of the main peak with a decreasing k, in which case the interference between the symmetric transitions and their resultant side peaks might occur.

In Fig. 7(c) a stronger field $V_0 = 0.05c^2$ is calculated, where at least five distinguished peaks can be observed. The main peak now is different from the peak in Fig. 7(a), because such a strong nonuniform field is able to affect the symmetric transitions and thus change the time evolution of the transition probabilities. In fact, as the Rabi frequency becomes comparable to the peak's width, we see the beginning of the Autler-Townes splitting [51–58]. On the other hand, two peaks corresponding to p_- and p_+ become wider as a result of a stronger amplitude of the spatially inhomogeneous field.

Finally, two more new peaks appear in Fig. 7(c): one at $E = 1.07c^2$ and the other at $E = 1.42c^2$. They are associated with the transition from $|p\rangle^-$ to $|p \pm 2k\rangle^+$. The

momentum and the energy of the maximum transition can also be determined by considering energy conservation. For these parameters they are $p_{--} = 54.9$ with corresponding energy $E_{--} = 1.07c^2$, and $p_{++} = 138.7$ with corresponding energy $E_{++} = 1.42c^2$, where p_{--} and p_{++} denote the resonant momenta involving transitions from $|p\rangle^-$ to $|p \pm 2k\rangle^+$. The energies E_{--} and E_{++} agree with the coordinates of the two new peaks in Fig. 7(c). Clearly, the above analytical solutions should be extended to reproduce the numerical results for strong fields. The impact of the spatially inhomogeneous field on the symmetric transition has not been taken into account, and one could also consider transitions involving $p \pm 2k$ for more accuracy.

VI. CORRELATION DIAGRAMS

In the Dirac equation simulation, the transition probabilities from each negative-energy state to each positive-energy state are calculated and presented in Fig. 8. In Fig. 8(a) we choose a weak amplitude $V_0 = 0.01c^2$, which can be solved analytically as we discussed in Sec. III. The horizontal axis is the positive energy and the vertical axis is the absolute value of the negative energy. The transition probabilities regarding certain states are indicated by the gray scale. The summation over every negative energy (the vertical axis) gives the energy spectra [Fig. 7(b)]; thus we are able to track the transitions leading to the peaks of Fig. 7 and identify those negative-energy states that are responsible for them in Fig. 8.

The "line" in the southwest-northeast facing diagonal denotes the symmetric transitions with identical momentum and symmetric energy, which is ascribed to the spatially uniform field. The maximum in the contour plot (spot) on the upper left is due to the asymmetric transition from $|p_+\rangle^-$ to $|p_-\rangle^+$. For the parameters we choose they are $p_+ = 122.3$ with $-E_{p_+} = -1.34c^2$ and $p_- = 80.4$ with $E_{p_-} = 1.16c^2$, which is exactly the coordinate of the spot. On the bottom right there is another spot which corresponds to the transition from $-E_{p_-} = -1.16c^2$ to $E_{p_+} = 1.34c^2$. Notice that the two spots and the center of the southwest diagonal ($E_p^- = -1.25c^2$ and $E_p = 1.25c^2$) are all located on the northwest-southeast diagonal, which indicates the energy conservation law when $E_p - E_p^- = \omega$.

For a stronger amplitude $V_0 = 0.05c^2$ in Fig. 8(b), the transitions involving p_- and p_+ are enhanced as more spots appear along the northwest-southeast diagonal, which corresponds to a wider width in Fig. 7(c). Also, at the upper-left corner and lower-right corner in Fig. 8(b), two more light spots can be identified, which are caused by the transitions to p_{--} and $p_{++}(= p_{--} + 2k)$, with energy $E_{--} = 1.07c^2$ and $E_{++} = 1.4c^2$, respectively. Due to energy conservation, the two new spots are also located on the southeast diagonal. One should note that the slight bending of "lines" in Fig. 8(b) is due to the nonlinear relationship between p and E_p. Overall, all of these structures in these correlation diagrams confirm the assumptions leading to the essential-state models discussed in Sec. III.

VII. CONCLUSIONS AND OUTLOOK

In this study we discussed the electron-positron pair-creation process triggered by a linear combination of a
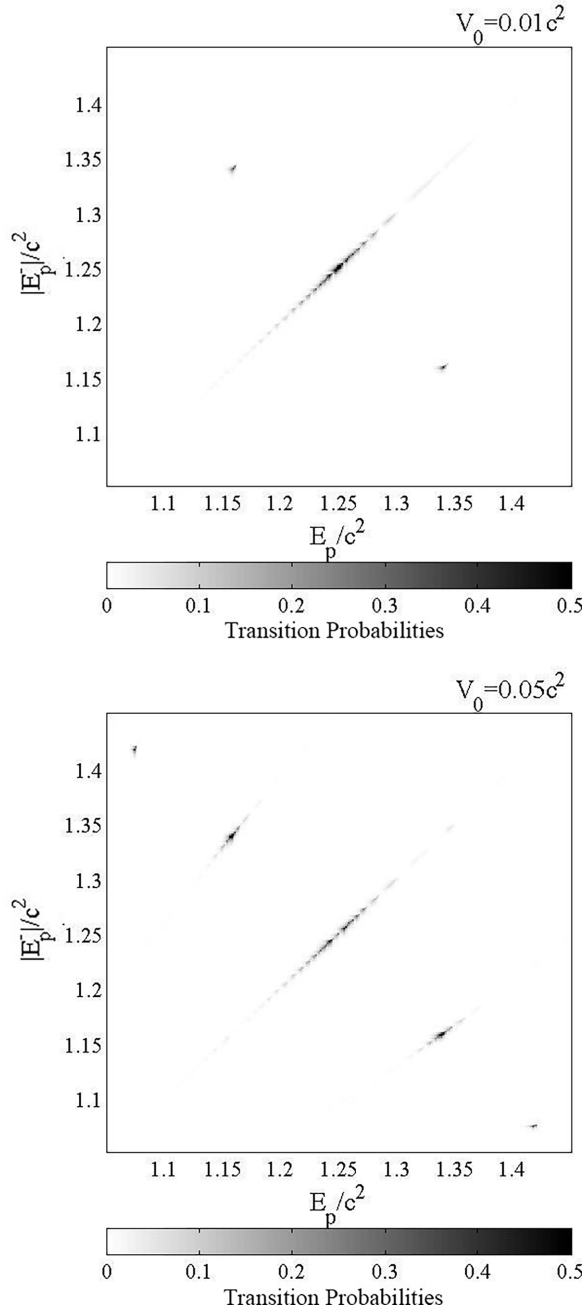
FIG. 8. The probability of transition between the negative and positive energy for $V_0 = 0.01c^2$ (a) and $V_0 = 0.05c^2$ (b) with $k = 41.9$. Parameters for the temporally oscillating field are $F_0 = 0.1c^3$ and $\omega = 2.5c^2$.

systems describing the transitions from the negative- to the final positive-energy Dirac states. Each of these four-level systems is characterized by an interesting interference of two pathways, while the direct (on-resonant) coupling between the initial and final state is negligible. Under the adiabatic elimination of the two intermediate levels, the dynamics can be reduced further to an effective two-level system, from which an analytical expression for the pair-creation rate was derived analytically. This rate scales quadratically with the product of the two amplitudes $(A_0 V_0)^2$, suggesting a symbiotic coupling between the temporal and spatial field.

While we examined a field configuration that was characterized by the simple sum of the two fields, the opening of the new vacuum decay channels is the result of a complicated interplay between the spatial and temporal degrees of freedom of both fields. A similar theoretical analysis based on an essential-state analysis could also be performed for a complimentary configuration where the spatial field modifies the temporal field in a multiplicative manner. For example, the resulting standing wave pattern of two cross-propagating laser beams would be an example of such a multiplicative space-time configuration.

It was predicted in the literature for the static Schwinger case (see many references in Ref. [31], in particular, [59–66]) that the inclusion of a spatial inhomogeneity often reduces the pair-creation yield. In our case of a temporally periodic field, we found an increase if the spatially inhomogeneous part is included in an additive manner.

We want to emphasize that our comparison does not solely revolve around the static Schwinger case. In our investigation the particle generation primarily arises from the temporal characteristics of the external field. Therefore our observed modification of the particle creation yield for our configuration is not a contradiction with literature [59–66], where the decrease is typically predicted for the Schwinger tunneling case. We note that only in the scenario of an infinite-photon limit, where each photon has zero energy, does our dynamics transition into the nonperturbative Schwinger limit. Mathematically, in this limit the traditional series expansion in the electric field becomes divergent. But using a Borel-like or other summation techniques, the nonperturbative Schwinger expression can be recovered as the sum of a diverging series [67].

The increase might be due to our choice of an additive spatial electric field. As a side issue, we note that if the additional spatial field can lead to a magnetic field [68–76] (which we have not considered), then, of course, the restriction of the associated particle orbits and new associated bound states might lead to a decrease of the yield. Similarly, if the spatial dependence is induced by the traveling wave character of a laser field, then often a yield decrease is observed. However, the question is nontrivial in our view. For example, we would like to mention here a very recent work [27] where the precise details of the spatial structure of two colliding laser fields can determine whether the yield actually increases or decreases. Clearly, we are not in the position yet to make any general statements about the suppressing or enhancing effect of spatially dependent fields for general interaction forms.

temporally and spatially periodic electric field and provided some general guidelines for studying more complicated configurations. For example, we extended the famous analytical Schwinger and Brezin-Itzykson multiphoton formulas for the pair-creation rate under temporally oscillatory electric fields into the regime of high photon energies.

For the case of an additional but weak spatially periodic field, the two-field dynamics leads to two additional peaks in the energy spectrum of the created positrons. The dynamics can be reduced to sets of mutually decoupled four-level

For the case of a temporally periodic field, the numerical data obtained from computational quantum field theory matched the ones obtained from the quantum Vlasov equation exactly. This exact description is based on the conservation of total momentum and the resulting description of the dynamics in terms mutually decoupled sets of two-level equations for each momentum. As the Vlasov equation is a powerful tool for spatially homogenous fields, it might be desirable in future studies to possibly extend its range of validity to include also more complicated configurations involving spatially inhomogeneous fields. While for the special case where the spatial inhomogeneity is periodic the total momentum is no longer conserved, we have shown that the dynamics can be still modelled by four-level systems. It is therefore anticipated that for weak spatial inhomogeneities we might be able to extend the Vlasov equations to accommodate space-time varying fields.

As we chose for numerical purposes a relatively small wavelength of about 20 Compton wavelengths for the spatial inhomogeneity, the resulting wave number k was quite large and comparable to the momentum of the created particles. As a result, the spatially induced energy peaks were clearly separated from the main peak associated with the symmetric momentum-conserving transition. However, as our essential-state analysis did not require such an energy separation, it might also be applied to the small-k case, where the final states populated via the symmetric and asymmetric transitions might have similar energies. We would expect in this regime the occurrence of new interesting interference mechanisms between the symmetric and asymmetric pathways. Overall, through this simple yet revealing model system and its quantitative analysis we hope to open opportunities for further studies. For example, it would be nice to see alternatives to probe the intriguing structure of the vacuum, either through a careful design of an electromagnetic field configuration that is best suitable for laboratory experiment or by making use of the magnetic field degree of freedom.

ACKNOWLEDGMENTS

APPENDIX A: SOLUTION FOR THE SYMMETRIC TRANSITION

In this Appendix we only consider the vector potential $A(t) = A_0 \cos(\omega t)$. The equations are

$$i\dot{C}_p^+(t) = [E_p^+ - a_p A_0 \cos(\omega t)]C_p^+(t)$$
$$- b_p A_0 \cos(\omega t)C_p^-(t),$$
$$i\dot{C}_p^-(t) = -b_p A_0 \cos(\omega t)C_p^+(t)$$
$$+ [E_p^- + a_p A_0 \cos(\omega t)]C_p^-(t). \quad \text{(A1)}$$

We set

$$C_p^+(t) = e^{-iE_p^+ t} e^{ia_p A_0 \int_0^t \cos(\omega \tau)d\tau} D_p^+(t). \quad \text{(A2)}$$

The left side of the first equation in Eq. (A1) is

$$i\dot{C}_p^+(t) = [E_p^+ - a_p A_0 \cos(\omega t)]C_p^+(t)$$
$$+ i\dot{D}_p^+(t)e^{-iE_p^+ t} e^{ia_p A_0 \int_0^t \cos(\omega \tau)d\tau}. \quad \text{(A3)}$$

Comparing with Eq. (A1), we have

$$i\dot{D}_p^+(t)e^{-iE_p^+ t} e^{ia_p A_0 \int_0^t \cos(\omega \tau)d\tau} = -b_p A_0 \cos(\omega t)C_p^-(t). \quad \text{(A4)}$$

By setting

$$C_p^-(t) = e^{-iE_p^- t} e^{-ia_p A_0 \int_0^t \cos(\omega \tau)d\tau} D_p^-(t) \quad \text{(A5)}$$

we obtain

$$\dot{D}_p^+(t) = \frac{i}{2}b_p A_0[e^{i(E_p^+ - E_p^- + \omega)t} + e^{i(E_p^+ - E_p^- - \omega)t}]$$
$$\times \sum_n J_n\left(\frac{-2a_p A_0}{\omega}\right)e^{in\omega t} D_p^-(t). \quad \text{(A6)}$$

Comparing to the zeroth order, which indicates a single-photon transition, other orders of the Bessel function are negligible in weak fields. Therefore we only consider the Bessel function J_0. For $E_p^+ - E_p^- - \omega \approx 0$ the first term oscillates with time and should be negligible, and thus we have

$$\dot{D}_p^+(t) = \frac{i}{2}b_p A_0 e^{i(E_p^+ - E_p^- - \omega)} J_0\left(\frac{-2a_p A_0}{\omega}\right)D_p^-(t). \quad \text{(A7)}$$

On the other hand, for $\dot{C}_p^-(t)$, by considering Eq. (A5), the left side of the second equation in Eq. (A1) is

$$i\dot{C}_p^-(t) = [E_p^- + a_p A_0 \cos(\omega t)]C_p^-(t) + i\dot{D}_p^-(t)e^{-iE_p^- t}$$
$$\times e^{-ia_p A_0 \int_0^t \cos(\omega \tau)d\tau}. \quad \text{(A8)}$$

Comparing with Eq. (A1) and considering Eq. (A5), we have

$$\dot{D}_p^-(t) = \frac{i}{2}b_p A_0[e^{i(E_p^- - E_p^+ + \omega)t} + e^{i(E_p^- - E_p^+ - \omega)t}]$$
$$\times \sum_n J_n\left(\frac{2a_p A_0}{\omega}\right)e^{in\omega t} D_p^+(t). \quad \text{(A9)}$$

Also, by only considering the Bessel function J_0 and ignoring the second term we obtain

$$\dot{D}_p^-(t) = \frac{i}{2}b_p A_0 e^{i(E_p^- - E_p^+ + \omega)t} J_0\left(\frac{2a_p A_0}{\omega}\right)D_p^+(t). \quad \text{(A10)}$$

Then we set $\tilde{D}_p^- = e^{i(E_p^+ - E_p^- - \omega)} D_p^-$, and according to Eqs. (A7) and (A10), we obtain

$$\dot{\tilde{D}}_p^-(t) = i(E_p^+ - E_p^- - \omega)\tilde{D}_p^- + \frac{i}{2}b_p A_0 J_0\left(\frac{2a_p A_0}{\omega}\right)D_p^+(t)$$
$$\dot{D}_p^+(t) = \frac{i}{2}b_p A_0 J_0\left(\frac{2a_p A_0}{\omega}\right)\tilde{D}_p^-(t). \quad \text{(A11)}$$

The final solutions are

$$\tilde{D}_p^-(t) = e^{i(E_p^+ - E_p^- - \omega)t/2} \Bigg[\cos\left(\frac{\Omega}{2}t\right)$$

$$+ i(E_p^+ - E_p^- - \omega)\frac{\sin\left(\frac{\Omega}{2}t\right)}{\Omega} \Bigg] \quad \text{(A12)}$$

$$D_p^+(t) = \frac{iA_0 b_p}{\Omega} J_0\left(\frac{2a_p A_0}{\omega}\right) e^{i(E_p^+ - E_p^- - \omega)t/2} \sin\left(\frac{\Omega}{2}t\right),$$

where $\Omega = \sqrt{(E_p^+ - E_p^- - \omega)^2 + A_0^2 b_p^2 J_0^2(\frac{2a_p A_0}{\omega})}$.

APPENDIX B: GENERAL ESSENTIAL STATE THEORY FOR ANY V_0

In a one-dimensional system, the Dirac Hamiltonian presented by a time-dependent vector potential $A(t)$ and a spatial periodic scalar potential $V(z)$ takes the form (in a.u.)

$$H = c\sigma_1 \left[p - \frac{A(t)}{c} \right] + c^2\sigma_3 + V(z)$$

$$= c\sigma_1 p + c^2\sigma_3 - \sigma_1 A(t) + V_0 \cos(kz)$$

$$= H_0 + W. \quad \text{(B1)}$$

The time evolution of a general state $|\phi(t)\rangle = \sum_p C_p^+(t)|p\rangle^+ + \sum_p C_p^-(t)|p\rangle^-$, satisfying the Dirac equation $i\frac{\partial}{\partial t}|\phi\rangle = H|\phi\rangle$. This means the expansion coefficients satisfy

$$i\sum_p \dot{C}_p^+(t)|p\rangle^+ + i\sum_p \dot{C}_p^-(t)|p\rangle^-$$

$$= \sum_p C_p^+(t)H_0|p\rangle^+ + \sum_p C_p^-(t)H_0|p\rangle^-$$

$$+ \sum_p C_p^+(t)W|p\rangle^+ + \sum_p C_p^-(t)W|p\rangle^-. \quad \text{(B2)}$$

By multiplying $^+\langle p_1|$ on the left and with the inner product $^+\langle p_1|p\rangle^+ = \delta(p_1 - p)$ and $^+\langle p_1|p\rangle^- = 0$, we obtain

$$i\dot{C}_{p_1}^+(t) = [E_{p_1} - a_{p_1}A(t)]C_{p_1}^+(t) - b_{p_1}A(t)C_{p_1}^-(t)$$

$$+ c_{p_1, p_1 \mp k}\frac{V_0}{2}C_{p_1 \mp k}^+(t) + d_{p_1, p_1 \mp k}\frac{V_0}{2}C_{p_1 \mp k}^-(t). \quad \text{(B3)}$$

Here E_p is the energy $\sqrt{c^4 + c^2 p^2}$ and $a_p \equiv {}^+\langle p|\sigma_1|p\rangle^+ = cp/E_p$, $b_p \equiv {}^+\langle p|\sigma_1|p\rangle^- = c^2/E_p$, $c_{p,p\mp k} \equiv {}^+\langle p|p \mp k\rangle^+ = [\sqrt{(E_{p\mp k} + c^2)(E_p + c^2)} + \sqrt{(E_{p\mp k} - c^2)(E_p - c^2)}] / (2\sqrt{E_{p\mp k}E_p})$, and $d_{p,p\mp k} \equiv {}^+\langle p|p \mp k\rangle^- = [\sqrt{(E_{p\mp k} + c^2)(E_p - c^2)} - \sqrt{(E_{p\mp k} - c^2)(E_p + c^2)}]/ (2\sqrt{E_{p\mp k}E_p})$. Very similarly, for the other amplitude $C_{p_1}^-(t)$ we have

$$i\dot{C}_{p_1}^-(t) = -b_{p_1}A(t)C_{p_1}^+(t) - [E_{p_1} - a_{p_1}A(t)]C_{p_1}^-(t)$$

$$- d_{p_1, p_1 \mp k}\frac{V_0}{2}C_{p_1 \mp k}^+(t) + c_{p_1 \mp k}\frac{V_0}{2}C_{p_1, p_1 \mp k}^-(t). \quad \text{(B4)}$$

With $c_{p,p\mp k} = c_{p\mp k,p}$ and $d_{p,p\mp k} = -d_{p\mp k,p}$, the equations of p that couple to $p - k$ and $p + k$ are

$$i\dot{C}_p^+(t) = [E_p - a_p A(t)]C_p^+(t) - b_p A(t)C_p^-(t)$$

$$+ c_{p,p-k}\frac{V_0}{2}C_{p-k}^+(t) + d_{p,p-k}\frac{V_0}{2}C_{p-k}^-(t)$$

$$+ c_{p,p+k}\frac{V_0}{2}C_{p+k}^+(t) + d_{p,p+k}\frac{V_0}{2}C_{p+k}^-(t),$$

$$i\dot{C}_p^-(t) = -b_p A(t)C_p^+(t) - [E_p - a_p A(t)]C_p^-(t)$$

$$- d_{p,p-k}\frac{V_0}{2}C_{p-k}^+(t) + c_{p,p-k}\frac{V_0}{2}C_{p-k}^-(t)$$

$$- d_{p,p+k}\frac{V_0}{2}C_{p+k}^+(t) + c_{p,p+k}\frac{V_0}{2}C_{p+k}^-(t),$$

$$i\dot{C}_{p-k}^+(t) = [E_{p-k} - a_{p-k}A(t)]C_{p-k}^+(t) - b_{p-k}A(t)C_{p-k}^-(t)$$

$$+ c_{p,p-k}\frac{V_0}{2}C_p^+(t) - d_{p,p-k}\frac{V_0}{2}C_p^-(t),$$

$$i\dot{C}_{p-k}^-(t) = -b_{p-k}A(t)C_{p-k}^+(t) - [E_{p-k} - a_{p-k}A(t)]C_{p-k}^-(t)$$

$$+ d_{p,p-k}\frac{V_0}{2}C_p^+(t) + c_{p,p-k}\frac{V_0}{2}C_p^-(t),$$

$$i\dot{C}_{p+k}^+(t) = [E_{p+k} - a_{p+k}A(t)]C_{p+k}^+(t) - b_{p+k}A(t)C_{p+k}^-(t)$$

$$+ c_{p,p+k}\frac{V_0}{2}C_p^+(t) - d_{p,p+k}\frac{V_0}{2}C_p^-(t),$$

$$i\dot{C}_{p+k}^-(t) = -b_{p+k}A(t)C_{p+k}^+(t) - [E_{p+k} - a_{p+k}A(t)]C_{p+k}^-(t)$$

$$+ d_{p,p+k}\frac{V_0}{2}C_p^+(t) + c_{p,p+k}\frac{V_0}{2}C_p^-(t). \quad \text{(B5)}$$

For the initial amplitudes $C_p^-(t = 0) = 1$, and all other amplitudes equal to zero, this set of coupled equations suggests the following coupling scheme: C_p^- couples first to C_p^+, C_{p-k}^-, C_{p+k}^-, C_{p-k}^+, and C_{p+k}^+. However, as the amplitudes with shifted momentum $p \pm k$ further activate transitions to amplitudes with momentums $p \pm 2k$, basically all states with momenta $p \pm nk$ get populated from $C_p^-(t = 0) = 1$.

APPENDIX C: REDUCTION TO TWO LEVELS FOR A WEAK V_0

In this Appendix we include the spatial part presented by $V(z) = V_0 \cos(kz)$. We focus on a transition between the negative state $|p\rangle$ and the positive state $|p + k\rangle$. For a very weak potential $V_0 = 0.01c^2$, the dynamics can be simplified to a four-level system:

$$i\dot{C}_p^-(t) = -[E_p - a_p A(t)]C_p^-(t) - b_p A(t)C_p^+(t)$$

$$+ c_{p,p+k}\frac{V_0}{2}C_{p+k}^-(t) - d_{p,p+k}\frac{V_0}{2}C_{p+k}^+(t),$$

$$i\dot{C}_p^+(t) = [E_p - a_p A(t)]C_p^+(t) - b_p A(t)C_p^-(t)$$

$$+ c_{p,p+k}\frac{V_0}{2}C_{p+k}^+(t) + d_{p,p+k}\frac{V_0}{2}C_{p+k}^-(t),$$

$$i\dot{C}_{p+k}^-(t) = -[E_{p+k} - a_{p+k}A(t)]C_{p+k}^-(t) - b_{p+k}A(t)C_{p+k}^+(t)$$

$$+ c_{p,p+k}\frac{V_0}{2}C_p^-(t) + d_{p,p+k}\frac{V_0}{2}C_p^+(t),$$

$$i\dot{C}_{p+k}^+(t) = [E_{p+k} - a_{p+k}A(t)]C_{p+k}^+(t) - b_{p+k}A(t)C_{p+k}^-(t)$$

$$+ c_{p,p+k}\frac{V_0}{2}C_p^+(t) - d_{p,p+k}\frac{V_0}{2}C_p^-(t). \quad \text{(C1)}$$

The factor $d_{p,p+k}$ is negligible compared to the other factors, so the last term on the right side of the equations can be removed. Then we apply a unitary transformation upon the states with the vector potential $A(t) = A_0 \cos(\omega t)$:

$$D_p^-(t) = e^{iE_p t - i\alpha_p \sin \omega t} C_p^-$$
$$D_p^+(t) = e^{-iE_p t + i\alpha_p \sin \omega t} C_p^+$$
$$D_{p+k}^-(t) = e^{iE_{p+k} t - i\alpha_{p+k} \sin \omega t} C_{p+k}^-$$
$$D_{p+k}^+(t) = e^{-iE_{p+k} t + i\alpha_{p+k} \sin \omega t} C_{p+k}^+. \tag{C2}$$

Here $\alpha_p \equiv a_p A_0/\omega$ and $\alpha_{p+k} \equiv a_{p+k} A_0/\omega$. If we only keep the zeroth order of the Bessel function, the equation of the state $|p\rangle^-$ in Eq. (C1) now becomes

$$i\dot{D}_p^-(t) = -\frac{b_p A_0}{2} J_0(2\alpha_p) e^{i(\omega - 2E_p)t} D_p^+(t)$$
$$+ \frac{c_{p,p+k} V_0}{2} J_0(\alpha_{p+k} - \alpha_p) e^{i(E_{p+k} - E_p)t} D_{p+k}^-(t). \tag{C3}$$

Then we introduce the exponential terms in front of $D_p^+(t)$ and $D_{p+k}^-(t)$ as

$$\tilde{D}_p^+(t) = e^{i(\omega - 2E_p)t} D_p^+(t)$$
$$\tilde{D}_{p+k}^-(t) = e^{i(E_{p+k} - E_p)t} D_{p+k}^-(t). \tag{C4}$$

After that, the equation of $|p^+\rangle$ becomes

$$i\dot{\tilde{D}}_p^+(t) = (2E_p - \omega)\tilde{D}_p^+(t) - \frac{b_p A_0}{2} J_0(2\alpha_p) D_p^-(t)$$
$$+ \frac{c_{p,p+k} V_0}{2} J_0(\alpha_{p+k} - \alpha_p) e^{i(\omega - E_p - E_{p+k})t} D_{p+k}^+(t). \tag{C5}$$

Notice that due to the exponential factor in the last term, the state $|p\rangle^+$ is again rotated as $\tilde{D}_{p+k}^+(t) = e^{i(\omega - E_p - E_{p+k})t} D_{p+k}^+(t)$. By applying all the rotations, the equations of the four-level system are

$$i\dot{D}_p^-(t) = -\frac{b_p A_0}{2} J_0(2\alpha_p)\tilde{D}_p^+(t)$$
$$+ \frac{c_{p,p+k} V_0}{2} J_0(\alpha_{p+k} - \alpha_p)\tilde{D}_{p+k}^-(t),$$

$$i\dot{\tilde{D}}_p^+(t) = (2E_p - \omega)\tilde{D}_p^+(t) - \frac{b_p A_0}{2} J_0(2\alpha_p) D_p^-(t)$$
$$+ \frac{c_{p,p+k} V_0}{2} J_0(\alpha_{p+k} - \alpha_p)\tilde{D}_{p+k}^+(t),$$

$$i\dot{\tilde{D}}_{p+k}^-(t) = (E_p - E_{p+k})\tilde{D}_{p+k}^- \tag{C6}$$
$$- \frac{b_{p+k} A_0}{2} J_0(2\alpha_{p+k})\tilde{D}_{p+k}^+(t)$$
$$+ \frac{c_{p,p+k} V_0}{2} J_0(\alpha_{p+k} - \alpha_p)\tilde{D}_p^-(t),$$

$$i\dot{\tilde{D}}_{p+k}^+(t) = (E_p + E_{p+k} - \omega)\tilde{D}_{p+k}^+(t)$$
$$- \frac{b_{p+k} A_0}{2} J_0(2\alpha_{p+k})\tilde{D}_{p+k}^-(t)$$
$$+ \frac{c_{p,p+k} V_0}{2} J_0(\alpha_{p+k} - \alpha_p)\tilde{D}_p^+(t).$$

Then we simplify the four-level system into a two-level system by assuming $\dot{\tilde{D}}_p^+(t) = 0$ and $\dot{\tilde{D}}_{p+k}^-(t) = 0$. In that case, according to Eq. (C6),

$$\tilde{D}_p^+(t) = -\frac{b_p A_0 J_0(2\alpha_p)}{2(\omega - 2E_p)} D_p^-(t)$$
$$+ \frac{c_{p,p+k} V_0 J_0(\alpha_{p+k} - \alpha_p)}{2(\omega - 2E_p)}\tilde{D}_{p+k}^+(t),$$

$$\tilde{D}_{p+k}^-(t) = -\frac{b_{p+k} A_0 J_0(2\alpha_{p+k})}{2(E_{p+k} - E_p)}\tilde{D}_{p+k}^+(t) \tag{C7}$$
$$+ \frac{c_{p,p+k} V_0 J_0(\alpha_{p+k} - \alpha_p)}{2(E_{p+k} - E_p)} D_p^-(t).$$

If we replace $\tilde{D}_p^+(t)$ and $\tilde{D}_{p+k}^-(t)$ in Eq. (C6) with Eq. (C7), the equations of the two-level system can be obtained as

$$i\dot{D}_p^-(t) = Q D_p^-(t) + R\tilde{D}_{p+k}^+(t),$$
$$i\dot{\tilde{D}}_{p+k}^+(t) = S\tilde{D}_{p+k}^+(t) + R D_p^-(t). \tag{C8}$$

The expressions of the coefficients in Eq. (C8) are

$$Q = \frac{b_p^2 A_0^2 J_0^2(2\alpha_p)}{4(\omega - 2E_p)} + \frac{c_{p,p+k}^2 V_0^2 J_0^2(\alpha_{p+k} - \alpha_p)}{4(E_{p+k} - E_p)},$$

$$R = -\frac{c_{p,p+k} V_0 A_0}{4} J_0(\alpha_{p+k} - \alpha_p)$$
$$\times \left[\frac{b_p J_0(2\alpha_p)}{\omega - 2E_p} + \frac{b_{p+k} J_0(2\alpha_{p+k})}{E_{p+k} - E_p} \right], \tag{C9}$$

$$S = (E_p + E_{p+k} - \omega) + \frac{b_{p+k}^2 A_0^2 J_0^2(2\alpha_{p+k})}{4(E_{p+k} - E_p)}$$
$$+ \frac{c_{p,p+k}^2 V_0^2 J_0^2(\alpha_{p+k} - \alpha_p)}{4(\omega - 2E_p)}.$$

According to Eq. (C8), the analytical solutions of the two-level system are

$$D_p^-(t) = e^{-\frac{i}{2}(Q+S)t}\left[\cos(\Omega t/2) + \frac{i(Q-S)}{\Omega}\sin(\Omega t/2) \right],$$

$$\tilde{D}_{p+k}^+(t) = -ie^{-\frac{i}{2}(Q+S)t}\frac{2R}{\Omega}\sin(\Omega t/2). \tag{C10}$$

Here $\Omega = \sqrt{4R^2 + (Q-S)^2}$. For the parameters considered in this paper, the value of the Bessel functions $J_0(2\alpha_p)$, $J_0(2\alpha_{p+k})$, and $J_0(\alpha_{p+k} - \alpha_p)$ are all very close to 1; thus the expressions of the coefficients Q, R, and S can be simplified to

$$Q = \frac{b_p^2 A_0^2}{4(\omega - 2E_p)} + \frac{c_{p,p+k}^2 V_0^2}{4(E_{p+k} - E_p)},$$

$$R = -\frac{c_{p,p+k} V_0 A_0}{4}\left(\frac{b_p}{\omega - 2E_p} + \frac{b_{p+k}}{E_{p+k} - E_p} \right),$$

$$S = (E_p + E_{p+k} - \omega) + \frac{b_{p+k}^2 A_0^2}{4(E_{p+k} - E_p)} + \frac{c_{p,p+k}^2 V_0^2}{4(\omega - 2E_p)}. \tag{C11}$$

[1] A. Di Piazza, C. Müller, K. Z. Hatsagortsyan, and C. H. Keitel, Extremely high-intensity laser interactions with fundamental quantum systems, Rev. Mod. Phys. **84**, 1177 (2012).

[2] B. S. Xie, Z. L. Li, and S. Tang, Electron-positron pair production in ultrastrong laser fields, Matter Radiat. Extremes **2**, 225 (2017).

[3] J. Schwinger, On gauge invariance and vacuum polarization, Phys. Rev. **82**, 664 (1951).

[4] G. A. Mourou, T. Tajima, and S. V. Bulanov, Optics in the relativistic regime, Rev. Mod. Phys. **78**, 309 (2006).

[5] T. Ditmire, High-power lasers, Am. Sci. **98**, 394 (2010).

[6] A. A. Voronin, A. M. Zheltikov, T. Ditmire, B. Rus, and G. Korn, Subexawatt few-cycle lightwave generation via multi-petawatt pulse compression, Opt. Commun. **291**, 299 (2013).

[7] N. Berrah and P. H. Bucksbaum, The ultimate x-ray machine, Sci. Am. **310**, 64 (2013).

[8] N. D. Powers, I. Ghebregziabher, G. Golovin, C. Liu, S. Chen, S. Banerjee, J. Zhang, and D. P. Umstadter, Quasi-monoenergetic and tunable X-rays from a laser-driven Compton light source, Nat. Photon. **8**, 28 (2014).

[9] C. N. Danson, C. Haefner, J. Bromage, T. Butcher, J.-C. F. Chanteloup, E. A. Chowdhury, A. Galvanauskas, L. A. Gizzi, J. Hein, D. I. Hillier et al., Petawatt and exawatt class lasers worldwide, High Power Laser Sci. Eng. **7**, e54 (2019).

[10] D. L. Burke, R. C. Field, G. Horton-Smith, J. E. Spencer, D. Walz, S. C. Berridge, W. M. Bugg, K. Shmakov, A. W. Weidemann, C. Bula et al., Positron Production in Multiphoton Light-by-Light Scattering, Phys. Rev. Lett. **79**, 1626 (1997).

[11] See https://eli-laser.eu; F. I. C. E. Turcu, F. Negoita, D. Jaroszynski, P. McKenna, S. Balascuta et al., High Field Physics and Qed Experiments At Eli-Np, Rom. Rep. Phys. **68**, S145 (2016).

[12] See, https://corels.ibs.re.kr.

[13] S. Meuren, E-20 collaboration at FACET-II, https://facet.slac.stanford.edu.

[14] C. Keitel, A. Di Piazza, G. Paulus, T. Stoehlker, E. Clark, S. Mangles, Z. Najmudin, K. Krushelnick, J. Schreiber, M. Borghesi, B. Dromey, M. Geissler, D. Riley, G. Sarri, and M. Zepf, Photo-induced pair production and strong field QED on Gemini, Mar 2021.

[15] See http://www.hibef.eu; H. Abramowicz, U. Acosta, M. Altarelli, R. Aßmann, Z. Bai, T. Behnke, Y. Benhammou, T. Blackburn, S. Boogert, O. Borysov et al., Conceptual design report for the LUXE experiment, Eur. Phys. J.: Spec. Top. **230**, 2445 (2021).

[16] Y. Kluger, J. M. Eisenberg, B. Svetitsky, F. Cooper, and E. Mottola, Pair Production in a Strong Electric Field, Phys. Rev. Lett. **67**, 2427 (1991).

[17] S. Schmidt, D. Blaschke, G. Röpke, S. A. Smolyansky, A. V. Prozorkevich, and V. D. Toneev, A quantum kinetic equation for particle production in the Schwinger mechanism, Int. J. Mod. Phys. E **07**, 709 (1998).

[18] Y. Kluger, E. Mottola, and J. M. Eisenberg, Quantum Vlasov equation and its Markov limit, Phys. Rev. D **58**, 125015 (1998).

[19] J. C. R. Bloch, V. A. Mizerny, A. V. Prozorkevich, C. D. Roberts, S. M. Schmidt, S. A. Smolyansky, and D. V. Vinnik, Pair creation: Back reactions and damping, Phys. Rev. D **60**, 116011 (1999).

[20] R. Alkofer, M. B. Hecht, C. D. Roberts, S. M. Schmidt, and D. V. Vinnik, Pair Creation and an X-Ray Free Electron Laser, Phys. Rev. Lett. **87**, 193902 (2001).

[21] S. P. Kim and C. Schubert, Nonadiabatic quantum Vlasov equation for Schwinger pair production, Phys. Rev. D **84**, 125028 (2011).

[22] F. Hebenstreit, R. Alkofer, and H. Gies, Particle Self-Bunching in the Schwinger Effect in Spacetime-Dependent Electric Fields, Phys. Rev. Lett. **107**, 180403 (2011).

[23] C. Kohlfürst, M. Mitter, G. von Winckel, F. Hebenstreit, and R. Alkofer, Optimizing the pulse shape for Schwinger pair production, Phys. Rev. D **88**, 045028 (2013).

[24] A. Di Piazza, Pair production at the focus of two equal and oppositely directed laser beams: The effect of the pulse shape, Phys. Rev. D **70**, 053013 (2004).

[25] S. S. Bulanov, V. D. Mur, N. B. Narozhny, J. Nees, and V. S. Popov, Multiple Colliding Electromagnetic Pulses: A Way to Lower the Threshold of e^+e^- Pair Production from Vacuum, Phys. Rev. Lett. **104**, 220404 (2010).

[26] C. K. Dumlu and G. V. Dunne, Interference effects in Schwinger vacuum pair production for time-dependent laser pulses, Phys. Rev. D **83**, 065028 (2011).

[27] C. Li, D. Su, Y. Li, Q. C. Su, and R. Grobe, Probing the spatial structure of the Dirac vacuum via phase-controlled colliding laser pulses, Europhys. Lett. **141**, 55001 (2023).

[28] H. Taya, H. Fujii, and K. Itakura, Finite pulse effects on e^+e^- pair creation from strong electric fields, Phys. Rev. D **90**, 014039 (2014).

[29] F. Gelis and N. Tanji, Schwinger mechanism revisited, Prog. Part. Nucl. Phys. **87**, 1 (2016).

[30] H. Hu, Seed and vacuum pair production in strong laser field, Contemp. Phys. **61**, 12 (2020).

[31] A. Fedotov, A. Ilderton, F. Karbstein, B. King, D. Seipt, H. Taya, and G. Torgrimsson, Advances in QED with intense background fields, Phys. Rep. **1010**, 1 (2023).

[32] C. Kohlfürst, The Heisenberg-Wigner formalism for transverse fields, arXiv:2212.06057.

[33] T. Cheng, Q. Su, and R. Grobe, Creation of multiple electron-positron pairs in arbitrary fields, Phys. Rev. A **80**, 013410 (2009).

[34] T. Cheng, Q. Su, and R. Grobe, Introductory review on quantum field theory with space-time resolution, Contemp. Phys. **51**, 315 (2010).

[35] Q. Su, Y. T. Li, and R. Grobe, Non-perturbative approach to bosonic multi-pair creation in arbitrary external fields, Laser Phys. **22**, 745 (2012).

[36] M. Alkhateeb, X. Gutiérrez de la Cal, M. Pons, D. Sokolovski, and A. Matzkin, Relativistic time-dependent quantum dynamics across supercritical barriers for Klein-Gordon and Dirac particles, Phys. Rev. A **103**, 042203 (2021).

[37] W. Greiner, B. Müller, and J. Rafelski, Quantum Electrodynamics of Strong Fields (Springer, New York, 1985).

[38] A. D. Bandrauk and H. Shen, High-order split-step exponential methods for solving coupled nonlinear Schrodinger equations, J. Phys. A: Math. Gen. **27**, 7147 (1994).

[39] J. W. Braun, Q. Su, and R. Grobe, Numerical approach to solve the time-dependent Dirac equation, Phys. Rev. A **59**, 604 (1999).

[40] U. Rathe, P. Sanders, and P. Knight, A case study in scalability: An ADI method for the two-dimensional time-dependent Dirac equation, Parallel Comput. **25**, 525 (1999).

[41] G. R. Mocken and C. H. Keitel, Quantum dynamics of relativistic electrons, J. Comput. Phys. **199**, 558 (2004).

[42] G. R. Mocken and C. H. Keitel, FFT-split-operator code for solving the Dirac equation in 2+1 dimensions, Comput. Phys. Commun. **178**, 868 (2008).

[43] C. C. Gerry, Q. Su, and R. Grobe, Timing of pair production in time-dependent force fields, Phys. Rev. A **74**, 044103 (2006).

[44] P. Krekora, Q. Su, and R. Grobe, Interpretational difficulties in quantum field theory, Phys. Rev. A **73**, 022114 (2006).

[45] R. Dabrowski and G. V. Dunne, Superadiabatic particle number in Schwinger and de Sitter particle production, Phys. Rev. D **90**, 025021 (2014).

[46] A. Ilderton, Physics of adiabatic particle number in the Schwinger effect, Phys. Rev. D **105**, 016021 (2022).

[47] C. Gong, Q. Su, and R. Grobe, Birth process of electron-positron pairs inside supercritical fields, Europhys. Lett. **141**, 65001 (2023).

[48] E. Brezin and C. Itzykson, Pair production in vacuum by an alternating field, Phys. Rev. D **2**, 1191 (1970).

[49] A. Huet, S. P. Kim, and C. Schubert, Vlasov equation for Schwinger pair production in a time-dependent electric field, Phys. Rev. D **90**, 125033 (2014).

[50] J. Unger, S. Dong, R. Flores, Q. Su, and R. Grobe, Relationship of the pair creation yield during and after the interaction, Laser Phys. **29**, 065302 (2019).

[51] S. H. Autler and C. H. Townes, Stark effect in rapidly varying fields, Phys. Rev. **100**, 703 (1955).

[52] P. L. Knight, AC Stark splitting of bound-continuum decays, J. Phys. B **12**, 3297 (1979).

[53] R. Grobe and J. H. Eberly, Observation of coherence transfer by electron-electron correlation, Phys. Rev. A **48**, 623 (1993).

[54] B. Walker, M. Kaluža, B. Sheehy, P. Agostini, and L. F. DiMauro, Observation of Continuum-Continuum Autler-Townes Splitting, Phys. Rev. Lett. **75**, 633 (1995).

[55] G. R. Mocken, M. Ruf, C. Müller, and C. H. Keitel, Nonperturbative multiphoton electron-positron-pair creation in laser fields, Phys. Rev. A **81**, 022122 (2010).

[56] B. Najjari, A. B. Voitkiv, and C. Müller, Two-Center Resonant Photoionization, Phys. Rev. Lett. **105**, 153002 (2010).

[57] C. Müller and A. B. Voitkiv, Resonant Two-Photon Single Ionization of Two Identical Atoms, Phys. Rev. Lett. **107**, 013001 (2011).

[58] D. D. Su, Y. T. Li, Q. Su, and R. Grobe, Laser-induced level shifts and splittings in multiphoton pair creation, Phys. Rev. D **103**, 074513 (2021).

[59] G. V. Dunne and C. Schubert, Worldline instantons and pair production in inhomogenous fields, Phys. Rev. D **72**, 105004 (2005).

[60] A. Ilderton, Localisation in worldline pair production and lightfront zero-modes, J. High Energy Phys. 09 (2014) 166.

[61] G. V. Dunne and Q.-H. Wang, Multidimensional worldline instantons, Phys. Rev. D **74**, 065015 (2006).

[62] G. V. Dunne, Q.-H. Wang, H. Gies, and C. Schubert, Worldline instantons and the fluctuation prefactor, Phys. Rev. D **73**, 065028 (2006).

[63] A. Nikishov, Barrier scattering in field theory removal of Klein paradox, Nucl. Phys. B **21**, 346 (1970).

[64] M. Ruf, G. R. Mocken, C. Müller, K. Z. Hatsagortsyan, and C. H. Keitel, Pair Production in Laser Fields Oscillating in Space and Time, Phys. Rev. Lett. **102**, 080402 (2009).

[65] H. Gies and G. Torgrimsson, Critical Schwinger Pair Production, Phys. Rev. Lett. **116**, 090406 (2016).

[66] H. Gies and G. Torgrimsson, Critical Schwinger pair production. II. Universality in the deeply critical regime, Phys. Rev. D **95**, 016001 (2017).

[67] G. V. Dunne, *QED Effective Actions in Inhomogeneous Backgrounds: Summing the Derivative Expansion*, AIP Conference Proceedings Vol. 564 (American Institute of Physics, Melville, NY, 2001), pp. 247–254.

[68] A. E. Shabad and V. V. Usov, γ-Quanta capture by magnetic field and pair creation suppression in pulsars, Nature (London) **295**, 215 (1982).

[69] J. K. Daugherty and A. K. Harding, Pair production in superstrong magnetic fields, Astrophys. J. **273**, 761 (1983).

[70] A. Di Piazza, Pair production in a strong rotating magnetic field: The effect of a weak background gravitational field, Int. J. Mod. Phys. A **21**, 251 (2006).

[71] Q. Su, W. Su, Q. Z. Lv, M. Jiang, X. Lu, Z. M. Sheng, and R. Grobe, Magnetic Control of the Pair Creation in Spatially Localized Supercritical Fields, Phys. Rev. Lett. **109**, 253202 (2012).

[72] W. Su, M. Jiang, Z. Q. Lv, Y. J. Li, Z. M. Sheng, R. Grobe, and Q. Su, Suppression of pair creation due to a steady magnetic field, Phys. Rev. A **86**, 013422 (2012).

[73] Q. Z. Lv, A. C. Su, M. Jiang, Y. J. Li, R. Grobe, and Q. Su, Pair creation for bosons in electric and magnetic fields, Phys. Rev. A **87**, 023416 (2013).

[74] M. Jiang, Q. Z. Lv, Y. Liu, R. Grobe, and Q. Su, Pair creation in localized electromagnetic fields of different spatial extensions, Phys. Rev. A **90**, 032101 (2014).

[75] G. Piccinelli and A. Sánchez, Magnetic field effect on charged scalar pair creation at finite temperature, Phys. Rev. D **96**, 076014 (2017).

[76] S. A. Alkhateeb, A. A. Alshaery, and R. A. Aldosary, Electron-positron pair production in electro-magnetic field, J. Appl. Math. Phys. **10**, 237 (2022).